

Experimental study and comparison of different geometric configurations in the reactive gases feeding of a PEMFC

C. M. Bautista-Rodríguez^{1,*}, Jennifer A. Bañuelos¹, A. de la Luz-Pedro¹,
María Maldonado Santoyo¹, Richard R. Lindeke².

¹ Centro de Innovación Aplicada en Tecnologías Competitivas (CIATEC). Dirección de Investigación y Desarrollo. Omega No. 201, Col. Industrial Delta, C.P. 37545, León, Guanajuato, México.

² Professor Emeritus, University of Minnesota Duluth, Volunteer/Collaborator with U.S. Peace Corps Mexico at CIATEC

* E-mail: cbautista@ciatec.mx

Received: 6 September 2017 / *Accepted:* 25 February 2018 / *Published:* 10 April 2018

Fuel cell technologies offers a real alternative for electrical energy generation, able to satisfy diverse portable and stationary services using today's technologies. Low temperature fuel cells (20-120 °C), particularly the Proton Exchange Membrane Fuel Cell (PEMFC), is a technology developed specifically for portable applications, while medium (200-600 °C) and high temperature (up to 1000 °C) systems are designed for stationary services. Multiple physical, electrochemical, kinetic and electrical phenomena occur during PEMFC operation. Specifically, the mass transport of reactants to reaction sites is fundamental to PEMFC operation and requires deeper understanding. When considering PEMFC fluid dynamics, significant pressure drop is observed when the geometry of the reactants' conducting surfaces is changed, this produces disturbances in both speed and flow profiles within the device. This work studies the effects of three factors that may significantly affect PEMFC functionality: (1) infeed geometry, for directing reactant gases to the distribution channels in the polar plates, (2) the type of flow (countercurrent and concurrent) for feeding reactants through the system, and (3) the level of cathode pressure in a PEMFC. Results from changing settings for these three factors have shown significant effects on PEMFC power and performance curves when the PEMFC was operated using various combinations of them during this study. Based on the observed test results, the team found that the best combination of operating conditions for PEMFC would be using high purity hydrogen and oxygen at a cathodic pressure of 10 psig using concurrent flow through venture-like intake and exhaust ports for the reactant gases. These operational conditions yield the best tested power performance (of about 0.78 W) at a current density of about 0.9 A/cm² in our experimental device.

Keywords: Flow Fluids, Mass Transport, PEMFC, Polar Plates, Power.

1. INTRODUCTION

Proton Exchange Membrane Fuel Cells (PEMFC) appear to be one of the most promising alternative power technologies [1-2] at the current time. Their main attractiveness includes zero pollutant emission and high electrical performance. Unlike conventional rechargeable batteries, PEMFC are not limited by lengthy off times during recharging. Fuel cells can be fed continuously from outside, so their operation is only limited by reactant feeding capacity and fuel availability. PEMFC also offer better energy transformation efficiency when connected to electric motors in electric powered vehicles [1-3]. Since 1996, many companies have worked to develop a low temperature PEMFC for integration in actual electric powered vehicles, some of these prototypes are capable of running at 120 Km/h with a range of 500 Km using a 30 kW Hydrogen/Air PEMFC fueled by hydrogen. PEMFC technology is also being applied to aquatic and space transportation, where the use of hybrid stationary systems can provide up to 2 MW of electric power [2].

A PEMFC is an electrochemical device that directly transforms chemical energy, using inverse hydrolysis reactions, to produce electrical energy. These reactions produce only water as a by-product while releasing heat [1, 3-10]. Low temperature PEMFC technology commonly uses hydrogen as fuel and oxygen as oxidant agent, operating at temperatures up to 120 °C, with pressures between 1 and 5 atmospheres [1, 4-6, 10]. A PEMFC single cell is constructed using a conductive proton membrane (commonly Nafion), two porous electrodes (anode and cathode respectively) with a catalytic charge, (commonly Platinum), two polar plates (graphite or metal) and two metallic supports.

Basically, the PEMFC's operation is centered on the electrodes and electrolyte. These elements are assembled in a thermo-pressure forming process producing the electrode-membrane-electrode (EME) interface. This assembly is then mounted between the polar plates [3, 5, 6, 9-14]. Beuscher [12] has proposed, in 2006, an experimental model to determine the mass transport resistance in a PEMFC, this model reports a concentration gradient of reactive gases through the thickness of the diffusion layer at the electrodes; the findings have suggested that gas distribution on the active layer of electrodes is not homogeneous. Hence polar plates are employed and they perform three functions in the PEMFC: 1) to provide homogenous distribution of reactant gases to the catalytic surfaces of the electrodes through channels machined therein. 2) collection of the electrons generated at the reaction points on the anode, cathode electrical reception to move them toward the surface of the cathode to complete the water generation reaction, and finally 3) to support the EME assembly [3, 4, 7, 13-15]. The role of the support plates are: 1) to provide mechanical support to the PEMFC, 2) to facilitate feeding of combustion gases, 3) to serve as temperature controls in the cell [1, 9, 10, 14].

Earlier studies [7-11, 13, 15-18] have reported on PEMFC performance at different levels of the operating variables including pressure, temperature, reactants' concentration, relative humidity conditions, and others. However, none of these studies has reported a direct fluid dynamic analysis to describe how fluid dynamics can affect the electrical current generated in the PEMFC. Some years ago, one of this manuscript's authors reported the effect of changing feeding direction of reactant gases on the

functionality in a PEMFC [19]. This paper, then, expands the knowledge of fluid dynamic effects of PEMFC performance, focusing on changes in the geometric configurations applied at the entrance to the gas flow channels in the polar plates on PEMFC functionality. In addition to these geometric studies, the study compares total PEMFC electrical generation when applying countercurrent versus concurrent flow for the reactant gases.

The ideal functionality of a fuel cell depends on the electrochemical reactions that take place in the active layer (catalyst) of the electrodes (anode and cathode). This functionality is defined by the Nernst's potential that represents the cell's electrical voltage (potential). The Nernst Eq. (1) develops the relationship between the ideal potential (E°) and the ideal equilibrium potential for different temperature and pressure conditions:

$$E = E^{\circ} + \frac{RT}{2F} \left[\ln \left(\frac{P_{H_2}}{P_{H_2O}} \right) + \ln \left(\sqrt{P_{O_2}} \right) \right] \quad (1)$$

Where: E is the cell potential, E° is the standard cell potential, T is the cell temperature, R is the universal gas constant, F is Faraday's constant and P is the gas pressure of fuel cell reactant or product species. In agreement with Nernst's equation for the oxidation-reduction reaction, the ideal electrical potential in an electrochemical (fuel) cell increases proportionately with the temperature and pressure. In a looped circuit, the cell's electrical potential is less than ideal electrical potential because of the irreversibility of the electrochemical reaction. This fact produces a deviation in the electrode's potential, with respect to its equilibrium potential, when the cell produces an electrical charge.

PEMFC functionality is characterized by a performance curve. The curve reflects different types of efficiency losses that are attributed to several issues. These losses include: 1) the irreversibility loss, resulting from over voltage at the electrodes resulting from the irreversibility of the electrochemical reactions, 2) the activation loss related to the electro-catalyst (commonly Pt) activity over the surface of the porous electrodes (typically observed at low current densities), 3) the ohmic loss, attributed to ionic and electronic resistances (typically observed at moderated current densities) and 4) the diffusion loss, caused by decreased concentration of the reactive gases on the active layer at the electrodes (typically observed at high current densities). Transport phenomena can also lead to loss of efficiency through competitive diffusion, of reactive gases, the water produced and other residuals gases, in the porous electrodes [1, 2-3, 5-8].

Reactant gases concentration over active sites in electrodes is fundamental to PEMFC functionality. Their concentration is a function of the different operating conditions including the infeed flow rate, flow temperature, flow pressure, relative humidity and specific gases distribution over the active surface of porous electrodes. In-feed takes place, conventionally, through distribution channels in the PEMFC polar plates. In these infeed channels, reactant gas transport conditions are defined by the fluid dynamics of the various gases (reactants and by-products). Typically the system is modelled by considering a uniform flow through a long straight pipe of constant diameter. Here the flow profile can be

modeled by the velocity distribution across the pipe's inner diameter. Starting with this simple arrangement the effect of any obstacle in the ideal pipe that changes the gases smooth flow characteristics, either partially or completely, which may introduce turbulence and, consequently, a loss of energy (pressure drop) greater than normally occurs in a totally straight pipe is added. Hence, energy loss can be determined by calculation of pressure drop for each flow section or determining the total coefficient of resistance to flow K , from individual coefficients for each section, pipe, valve and/or accessory in the system [20-22]. The flow resistance factor K is defined as:

$$K_2 = K_1 \left(\frac{d_2}{d_1} \right)^4 \quad (2)$$

Where, the subscript "2" defines K and d (inner diameter) of the outlet pipe in question. The subscript "1" defines K and d (inner diameter) of the inlet pipe (where a known value of K has been computed earlier).

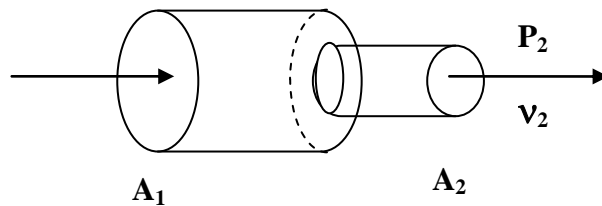


Figure 1. Schematic of Sudden Contraction

In a sudden contraction case, as in Figure 1, P_1 pressure is greater P_2 since input stream velocity v_1 is lower than the output velocity v_2 , ($v_1 < v_2$) as based on the Bernoulli effect, so it defines a velocity profile for the specified arrangement [20]. The following mathematical expressions are considered [ref. 20-22] for sudden expansion or contraction cases:

For contractions: $K_1 = 0.5(1 - \beta^2)$ (3)

For expansions: $K_1 = (1 - \beta^2)^2$ (4)

Where β represents the (d_2/d_1) ratio.

For contractions or expansions in Venturi-type pipes, as shown in Figure 2, the following mathematical expressions are developed:

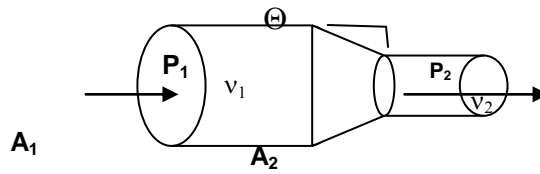


Figure 2. Schematic for a Venturi array.

For contractions where $\Theta = 45^\circ$, K_2 is modeled by Eqn. 5:

$$K_2 = \frac{0.8 \sin \frac{\Theta}{2} (1 - \beta^2)}{\beta^4} \quad (5)$$

For expansions where $\Theta = 45^\circ$ (inverse flow than that shown in Figure 2), K_2 is modeled by Eqn. 6:

$$K_2 = \frac{2.6 \sin \frac{\Theta}{2} (1 - \beta^2)^2}{\beta^4} \quad (6)$$

Continuing, head (load) loss h_L , in valves and accessories, is defined by Darcy equation:

$$h_L = f \frac{L}{D} \frac{v^2}{2g_n} \quad (7)$$

Here we define: $K = f \frac{L}{D}$ (8)

g_n is gravity constant and f is the appropriate friction factor, L is the (longer) channel length and D is the channel diameter

Eq. (9) and Eq. (10), respectively, defining the average flow velocity and the pressure drop in a Venturi array:

$$v = \frac{\omega}{A * \rho} \quad (9)$$

$$\Delta P = \frac{h_L \rho}{10200} \quad (10)$$

Where ω is the mass gas flowrate, A is the transport area and ρ is the gas density during transport.

It is known that pressure loss, the specific flow profiles, and reactant gases velocity in polar plate distribution channels may generate significant concentration gradients on the active layer of electrodes and, consequently, may have a significant effect on the PEMFC's functionality.

2. EXPERIMENTAL STUDIES

2.1 Electrochemical System

Two structural PEMFC has been designed. Each of them can be mounted with different polar plate and support plate sets. The EME assemblages were thermoformed using commercial electrodes (from E-teck). The electrodes are fashioned from carbon (graphite) fabric, that provides mechanical resistance and electrical conductivity, and covered with a carbon powder (type Vulcan XC-72) supporting nanoparticles of Platinum (Pt). The Pt-catalyst charge was 0.4 mg/cm^2 and only present, as an active layer, in contact with the electrolyte. A Nafion® 115 film was used as the electrolytic membrane. The electrolyte had an effective mass area of 0.7 mg/cm^2 [9, 17]. This film was $100 \text{ }\mu\text{m}$ thick (before activation) and $120 \text{ }\mu\text{m}$ thick (after activation). The active area of the ECE membrane after thermoforming is $1.41 \times 1.41 \text{ cm}$. All these conditions are similar to those found in PEMFC references [6, 9-10]. The total electrolyte area was equivalent to 25 cm^2 ($5 \times 5 \text{ cm}$). Combustible and oxidant gases employed were high purity hydrogen and oxygen (both 99%, INFRA), respectively.

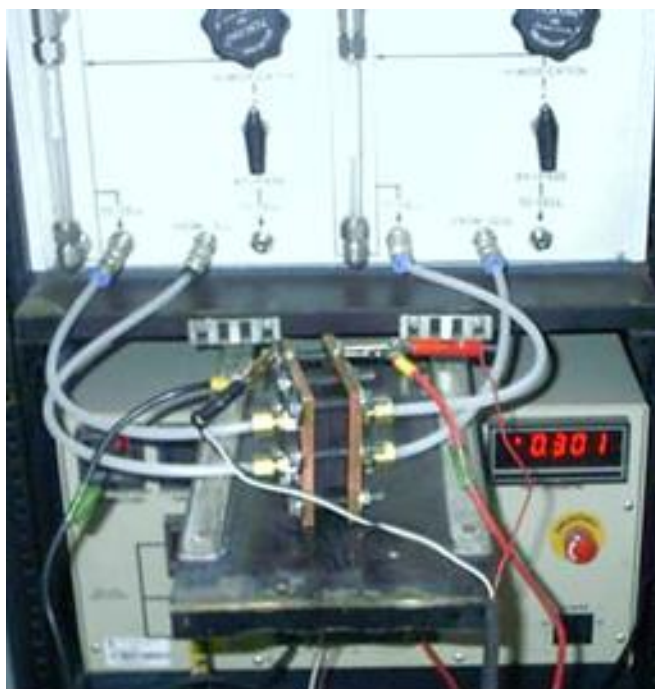


Figure 3. PEMFC connected in a test bench.

Figure 3 shows the experimental mono-cell and connections in a “Fuel Cell Test System Globe Tech Compu-Cell GT-890-B” for studying the performance characterization and Figure 4 shows the countercurrent and/or concurrent flows to feed the reactant gases. Table 1 describes the experimental conditions applied.

Table 1. Operating conditions on the PEMFC.

Variables (units)	Anode	Cathode
Gas flow (cc/min)	50	50
Pressure (psi)	4	4,6,10 and 14
Humidity temperature (°C)	35	35
Cell temperature (°C)	room	room

2.1.1 Flow Profiles Applied

Figure 4 is a schematic of the applied flow profiles. In both 4a and 4b the EME assembly is located at the center of each sketch while on both sides are found the reactant gas distribution channels. The arrows indicate, on the one hand, the distribution of the reactive gases along the serpentine channels and on the other hand, their distribution to the surface of the porous electrodes.

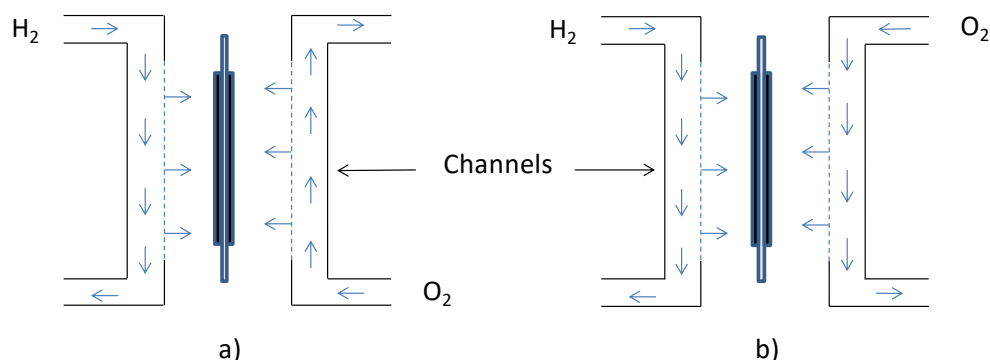
**Figure 4.** Flow profile sketch for a) countercurrent and b) concurrent flows

Figure 4.a shows the flow profile of the countercurrent reactive gas flow; here the flow of hydrogen enters through the top of the polar distribution plate while the oxygen enters the bottom of the polar plate on the opposite side of the EME. Under these conditions, each of the reactants concentration is reduced from the channel inlet in the direction to the outlet by consumption on the porous electrodes. And since this concentration reduction is carried out in the opposite direction between both gas flows, hypothetically, random potential gradients on the electrode surfaces will be generated.

Figure 4.b shows the flow profile of the reactive gases under concurrent flow, thus both reagents enter the top of the distribution plates' serpentine channels, reducing the concentration of the reactants similarly along the channels by consumption on the porous electrodes. Hypothetically, a potential gradient is likely between the channels entry region and exit region of the EME assembly.

2.2 Geometry of the 'sudden contraction' in polar plates

On the first polar plate set, a sudden contraction at the inlet and outlet of reactive gases compartments was machined for the anode and cathode (see Figure. 53). To accomplish this sharp change, the feed diameter in the copper metallic supports was machined to 9 mm whereas in the graphite polar plates, leading to the serpentine channels, it is only 3 mm to provide a choke in the inflow.

2.3 Geometry for a Venturi-like contraction in polar plates

On the second polar plate set, a Venturi-like tube geometry was machined for the reactant gas inlet and outlet compartments. The geometry was designed to introduce a smoother flow with more regular velocity profiles for conducting reactive gases as they are introduced into the respective anodic or cathodic compartments and subsequently into the outlet pipes. Figure 5 presents a schematic view of this Venturi-like arrangement, as well as the sudden constriction geometries. In the venturi-like plate geometries, at the inlet end, the 9mm tubes are coupled to the 6 mm venturi-like inlet channel that carries the gases through a 45° contraction zone to the 3mm inlet tube that couples, in turn, to the serpentine channels in the polar plates. At the outlet end the serpentine channel couples to the graphite plates employing a 3 mm the outfeed tube which in turn leads to a 6 mm diameter tube, over a 45° expansion angle, before mating to the outflow tube of 9 mm.

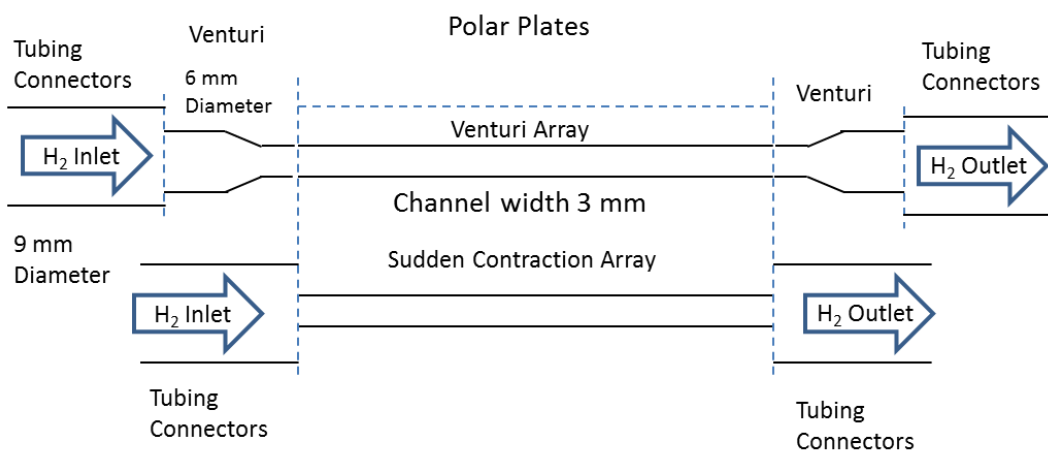


Figure 5. Structural sketch for sudden contraction and Venturi arrays

3. RESULTS AND DISCUSSION

3.1 Oxygen flow velocity profile

Figure 6 shows the velocity profile for the hydrogen inflow feed in the 2 different geometric configurations applied in this study. It is important to observe the reduction of the slope in the infeed

velocity over the first section of the Venturi-like array (VA) when compared to that observed in the sudden contraction array (SCA), these flow profiles suggest less turbulence and potentially reduced pressure losses over the initial zone.

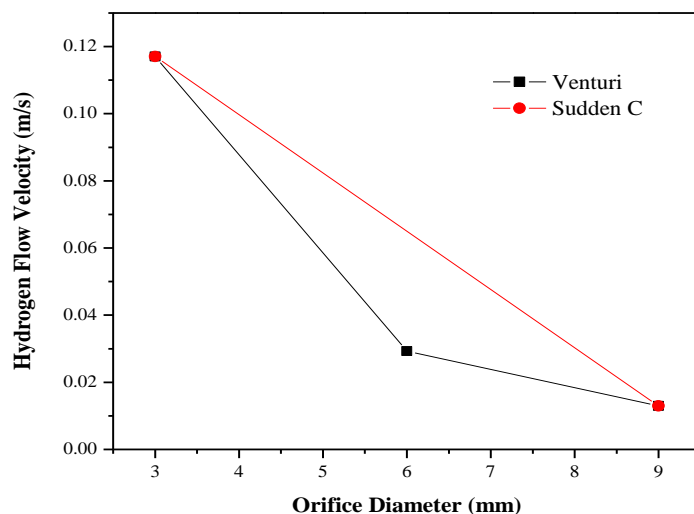


Figure 6. Velocity profile for hydrogen inlet inside VA and SCA (and note, the actual inflow starts at the right side of the graph (9 mm D) and proceeds through to the polar plate channels (3 mm D))

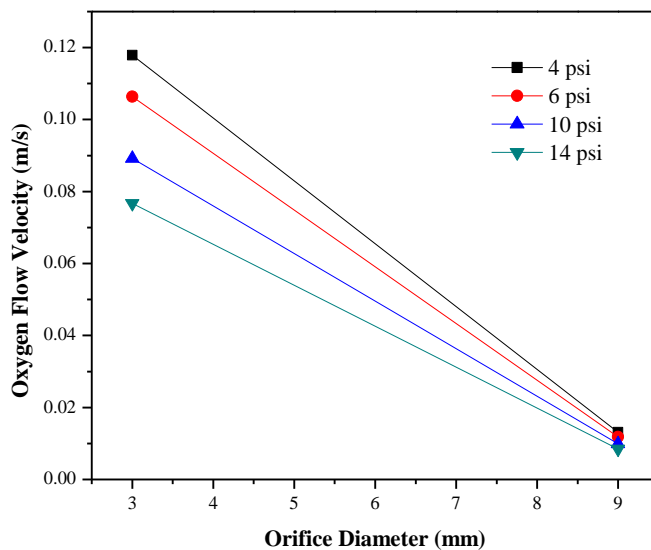


Figure 7a. Oxygen flow velocity profile at the inlet of the cathodic distribution plate for a sudden contraction

Velocity profiles for oxygen infeed flows, using the SCA at different applied PEMFC cathode pressure, are shown in Figure 7a. Figure 7b presents the velocity profiles, when the VA was employed, for cathodic infeeding at these same pressure conditions.

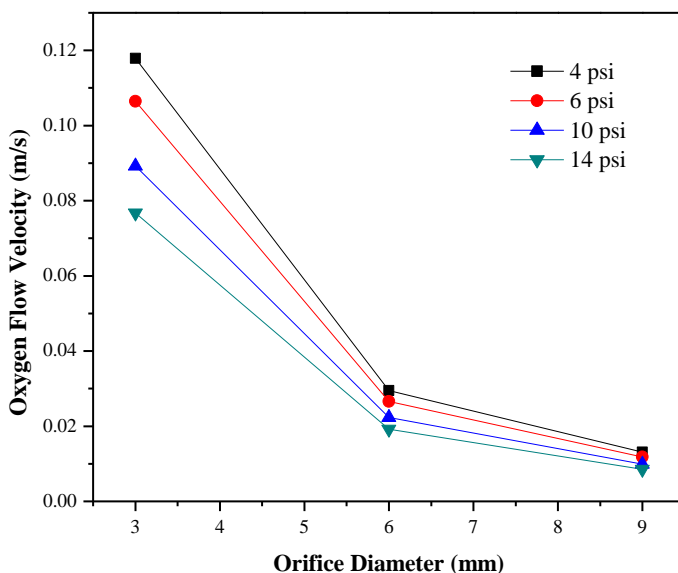


Figure 7b. Oxygen flow velocity profile at the inlet of the cathodic distribution plate for VA

Regardless of the geometry employed for the inlet the velocity profile for Oxygen and Hydrogen displayed similar behavior as seen in Figure 6 and Figure 7. However, reduction in speed, as pressure was increased, was unexpected. It is likely that this behavior can be attributed to an increase in gas density, due to compression, at higher oxygen pressure in the PEMFC cathodic compartment. Consequently, lower turbulence levels can be expected when pressure is increased leading to a better feed profile to the active surface of the electrode.

Khac et al., reported simulation model results versus experimental data for a PEMFC in operation [23], their PEMFC used similar conditions for the EME and polar plates with concurrent and countercurrent flow as in this study. The simulation results shows that gas velocity profiles, comparing between concurrent or countercurrent flow modes, exhibited some minor differences. In addition, the hydrogen mass fraction increased along the anodic electrode surface between inlet and outlet, which indicated that the drag induced by the flux of water within the EME is higher than the hydrogen consumption rate. On the cathodic side the oxygen mass fraction is quasi-homogeneous due to its stoichiometric excess in the reaction. These effect were reports for either flow type.

Table 2. Estimation of flow parameters for oxygen inside the cathodic chamber during the SCA study case

Parameter (units)	3 mm 4 psi	9 mm 4 psi	3 mm 6 psi	9 mm 6 psi	3 mm 10 psi	9 mm 10 psi	3 mm 14 psi	9 mm 14 psi
Density (lb/ft ³)	0.0226	0.0226	0.0339	0.0339	0.0565	0.0565	0.0791	0.0791
Reynolds number	6.27	2.09	9.41	3.14	15.68	5.23	21.96	7.32

Table 2 presents density and Reynolds number estimation for oxygen flow inside the cathodic channels when the SCA was employed. Oxygen density values directly increased as the pressure level imposed at the cathode increased, however no significant change in density is observed as a function of diameter on either side of the SCA at the same cathode pressure. This behavior is attributed at the molecular proximity caused by a pressure increase, which is not significantly affected by flow diameter in the SCA. Reynolds number increased moderately when pressure was increased. Considering the 9 mm diameter infeed tube it showed small increases but this increase was much greater once it was computed inside the 3 mm diameter distribution channel. We note, too, that while much higher Reynolds numbers were computed for the highest pressure in the 3mm channel, none of the values suggested an entry into a turbu

Table 3 presents density and Reynolds number estimation for oxygen flow when the gas is introduced into the cathode compartment using the VA geometry. Here, similar behaviors as found for the SCA geometry are observed. Table 3 also includes computed values at the intermediate diameter (6mm) for the Venturi-like design. Note that here, density and Reynolds number behavior was identical to SCA values. Apparently, neither of the chosen geometries has a significant effect on the characteristics of the oxidizing feed gas and thus do not likely has differing significant effects on the function of the PEMFC.

Table 3. Estimation of flow parameters for oxygen inside the cathodic chamber during VA study case

Parameter (units)	3 mm 4 psi	6 mm 4 psi	9 mm 4 psi	3 mm 6 psi	6 mm 6 psi	9 mm 6 psi	3 mm 10 psi	6 mm 10 psi	9 mm 10 psi	3 mm 14 psi	6 mm 14 psi	9 mm 14 psi
Density (lb/ft ³)	0.0226	0.0226	0.0226	0.0339	0.0339	0.0339	0.0565	0.0565	0.0565	0.0791	0.0791	0.0791
Reynold number	6.27	3.14	2.09	9.41	4.70	3.14	15.68	7.84	5.23	21.96	10.97	7.32

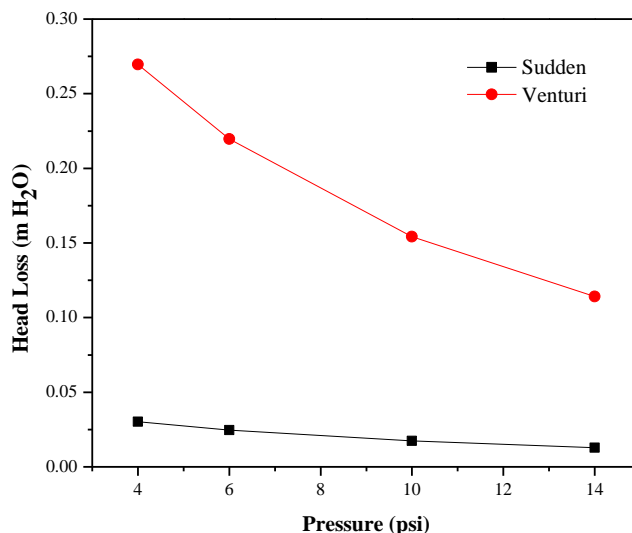


Figure 8. Head losses (pressure drop) in sudden contraction and Venturi array

Figure 8 graphs pressure losses for the oxygen flow when comparing the geometric designs under study. Remarkably, the pressure drop for the VA was greater than observed for the SCA design. Here, the pressure losses followed an exponential behavior as operation pressures increased for the VA. While it is lower, the pressure loss found with the SCA design, displayed a quasi-linear behavior, even when higher operating cathode pressures are imposed. Based on the pressure loss behavior, it is expected that these flow pressure drops may have a significant effect on the PEMFC performance.

3.2 PEMFC functionality

The PEMFC’s functionality curves for VA and SCA are shown in Figure 9a and Figure 9b. In both cases, the catalytic activation zone is observed between 0 and 0.05 A/cm². The ohmic losses zone is observed at values between 0.5 and 1.1 A/cm² and no significantly difference in the performance is observed between SCA or VA over this section as any given pressure. Finally, the gas diffusion loss zone is observed to be nearly identical regardless of the structural design used. The several functionality curves in both figures obey Nernst’s law when concurrent flow was used.

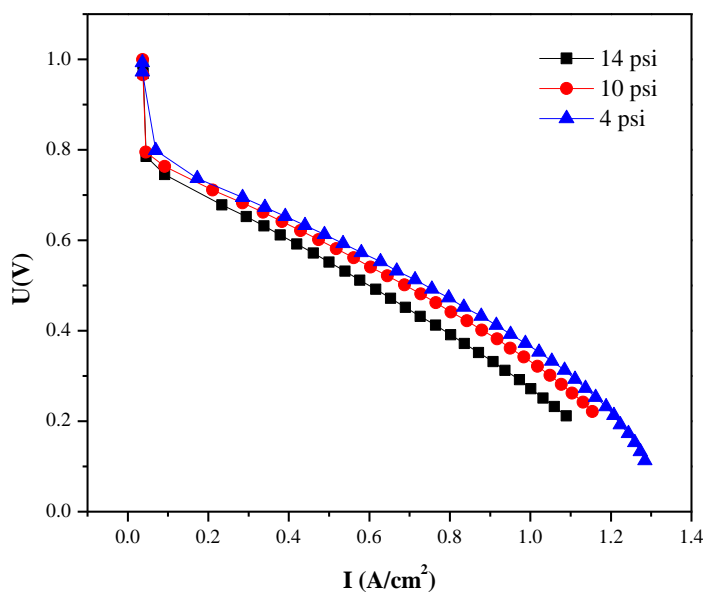


Figure 9a. Performance curves for PEMFC using sudden contraction array at different pressure levels in the cathodic distribution plate and concurrent gases flow.

To more readily compare the differences in the PEMFC performance curves when employing either the VA and the SCA geometries under concurrent flow, Figure 10 was developed show both in a single graph. Here only two different cathode compartment pressure levels (4 and 10 psi) are included. Since pressure drop is higher when the VA was employed (Figure 8) the team expected that PEMFC performance loss to be greater for all pressure levels applied when using the VA geometry.

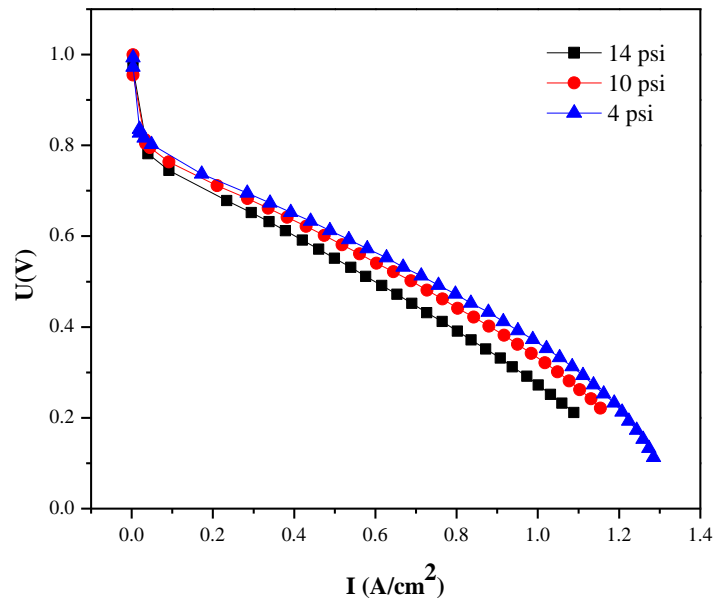


Figure 9b. Performance curves for PEMFC using Venturi array at different pressure levels in the cathodic distribution plate and countercurrent gases flow.

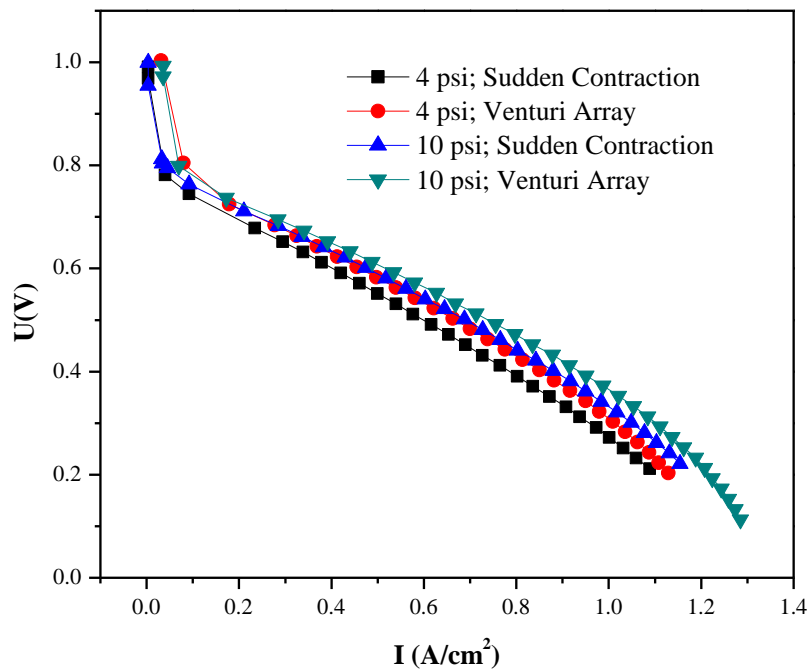


Figure 10. Performance curves for PEMFC using different feed mechanical structures at different pressure levels in the cathodic distribution plate and concurrent gases flow.

However, the highest current densities were observed when the VA geometry was employed. This behavior may be attributable to improved feed conditions using VA, however this advantage is not strongly supported by the flow calculations presented.

Figure 11 show the functionality curves for PEMFC using VA geometry with countercurrent flow over the different cathodic pressure levels. Different behaviors are observed with counter flowing VA compared to those observed with the concurrent flow conditions. 1) The activation zone appeared shorter and was not well defined between 0 and 0.05 A/cm^2 , this suggests a different electrode activation process using a counter-flow VA system. 2) The ohmic losses zone finishes at approximately 1.2 A/cm^2 , showing a notable linearity and higher slope compared to the concurrent flow case, it is possibly caused by an increase in electrical resistance at the electrode-electrolyte interface. 3) A diffusion zone is observed between 1.1 and 1.35 A/cm^2 . Here, it is important to observe that at all cathodic chamber pressures tested, the current density is reduced by about 0.2 A/cm^2 compared to the concurrent flow case. Thus an increase in diffusion resistance for the reactive gases can be deduced when countercurrent flow is employed. Finally, PEMFC performance curves decreased inversely as a function of pressure level when using VA combined with countercurrent flow, attributable at pressure losses when operating at these conditions.

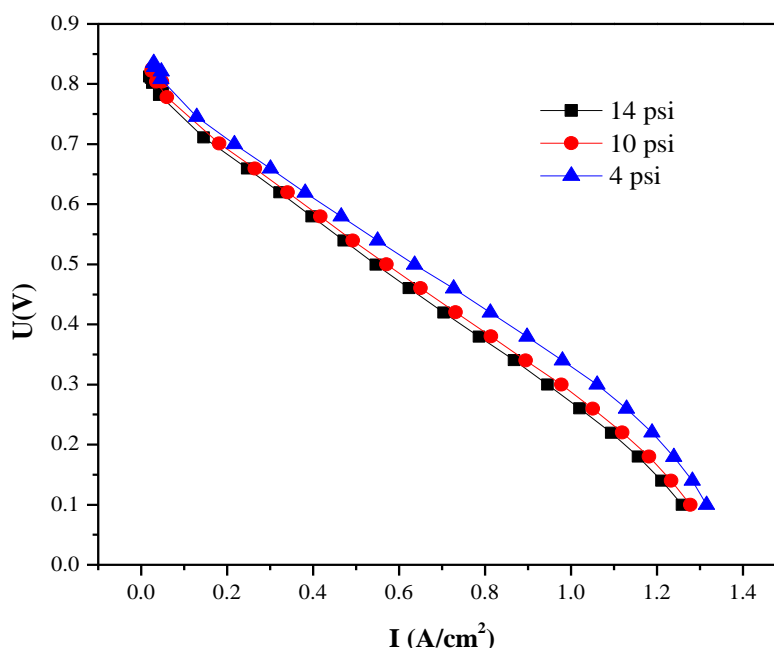


Figure 11. Performance curves for PEMFC with VA at different pressure levels on the cathodic distribution plate and countercurrent gas flow.

There was expected to be a greater tendency for over potential due to reactant concentration on the active layer in the electrodes during countercurrent flow conditions. Note that in a counterflow system higher concentrations of hydrogen are “matched” with lower concentrations of oxygen (and visa-versa). In this type of flow, the gradient concentration is expected to be higher than for concurrent flows. This is a

function of the distribution of reactants, pressure drop (Pinlet-Poutlet) in the channels, flow velocity and flow profile over the surface of porous electrodes. If the expected over potential conditions actually developed, the power and performance curves for the PEMFC were expected to be negatively affected as predicted by the Nernst Law. But this was, unexpectedly, not observed in the Figure 11 suggesting that this flow condition did not lead to any significant change in over potential compared to concurrent flows.

Zeroual et al., [24] developed an isothermal and unsteady three-dimensional model to study the influence of physical and geometric parameters, gas flows in the distribution channels, and reagent consumption in a PEMFC. They concluded that consumption of reagents becomes more uniform by reducing the rate of gas flow in the channels, which leads to a more uniform current density. Using wider channels with thinner ribs lead to more uniform consumption and a better performing PEMFC. Low flow rates may be obtained at reduced pressure level, so the results in Figure 11 may be attributed to the combined interactions of the pressure levels as well as geometric pattern driving gas flows over the EME as suggested by Zeroual, et al.

Performance curve effects, considering the different reactant gas feeding techniques, are presented in Figure 12. The increase of the PEMFC efficiency is somewhat improved for concurrent flow with VA as compared to SCA. Similar behavior is observed in activation zone ($0 - 0.1 \text{ A/cm}^2$) on both curves, while performance, using SCA and concurrent flow, exhibited higher ohmic and diffusion resistances.

On the other hand, the performance curve for VA under countercurrent flow is notably different in all zones. Particularly in the activation zone results suggest a different activation mechanism than with concurrent flows. This behavior is attributed to electro-catalytic activation as function of feed direction and the concentration of reactive gases over the active layer of electrodes. The slope of the PEMFC's functionality curve suggests an increase in ohmic resistances, again attributable to reactive gas concentration gradients on the surface of electrodes as the gas consumption changes caused by the mismatched cross EME concentrations. Here, the membrane water content which is the reaction product is heterogeneous on the active layer when compared to concurrent flow. Thus since the membrane's humidity is (likely) heterogeneous it leads to different ionic resistance in the membrane. One can observe that as current density exceed about 1.0 A/cm^2 that an optimal electrolyte water saturation is achieved, which favors ionic conductivity, leading to current densities that exceed the concurrent flow cases. In this condition, mass transport resistance decrease significantly, allowing electrical density increases as seen in the performance curve.

Khac et al., [23] have reported similar results, reporting current density variations, in the fuel cell operating at 0.6V, noting increases in measurement taken from the center of PEMFC to the edges of the polar plates. This variation is attributed to hydrogen flow velocity through the gas channel. They also showed that the current density distribution of the concurrent and countercurrent mode indicates no significant change due to the gas flow patterns at wet conditions. However, they found that the dry reactant gases can will be well humidified during PEMFC operation, and maintain high performance, when using the countercurrent mode without any external humidification being required. In our studies

with counterflow, the hydrogen stream may be have been well-hydrated at low and medium current density but at high densities is probably would have been.

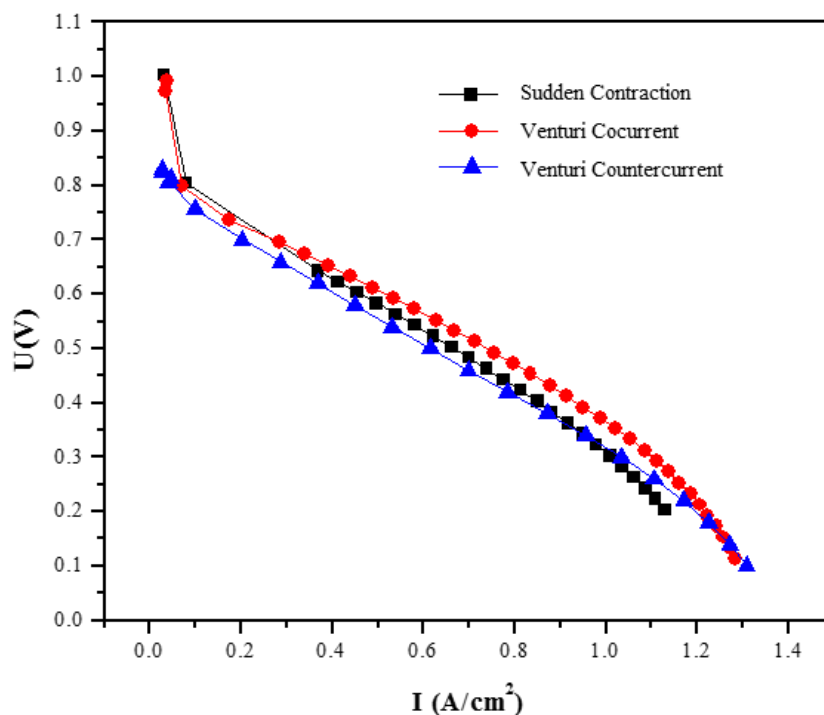


Figure 12. Performance curves at 4 psi of cathodic pressure in the PEMFC with different geometry arrays for the inlet gases to the polar plates.

In another report, Morin et al. [25], demonstrated the effect from concurrent or countercurrent flow configuration on PEMFC performance as well. While testing, they used ‘pure’ hydrogen and oxygen and operating at 80 °C and current densities of 400 and 800 mA/cm². Their polar plates were machined with gas distribution channels 1.2 mm in both width and depth and a rib thickness of 0.8 mm. During their reported tests, the best PEMFC performance was obtained using countercurrent flow which they attributed to a more homogeneous membrane hydration level. In concurrent flow, the membrane was reported to be very dry, near the gas inlets, but fully hydrated at the gas outlets. When comparing their study to ours where we employed distribution channels that were 3 mm X 3mm (width and depth) and a 2 mm rib thickness, the PEMFC of Morin et al. was more sensitive to water management phenomena and its effects on membrane hydration. In our case, the expanded channel size offered greater humidity exhaust under countercurrent flow leading to increased membrane dryness until high current densities (>1A/cm²) were observed.

3.3 PEMFC power performance

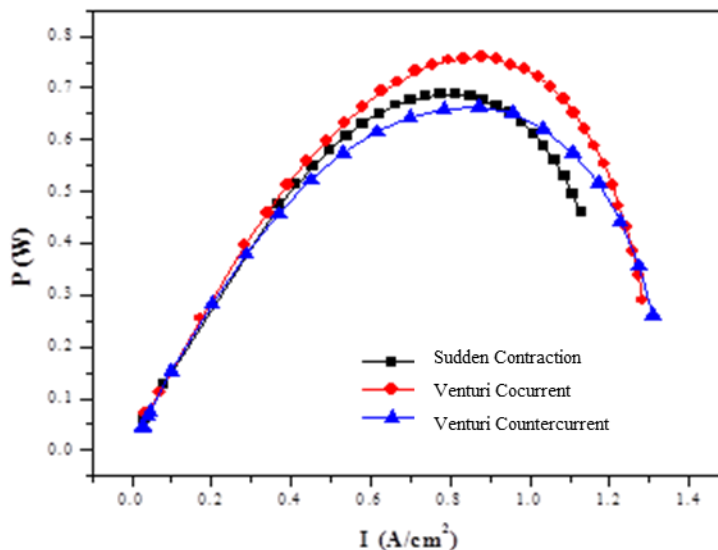


Figure 13. Power curve for a PEMFC at 4 psi cathodic pressure for different structural arrays and inlet flow patterns.

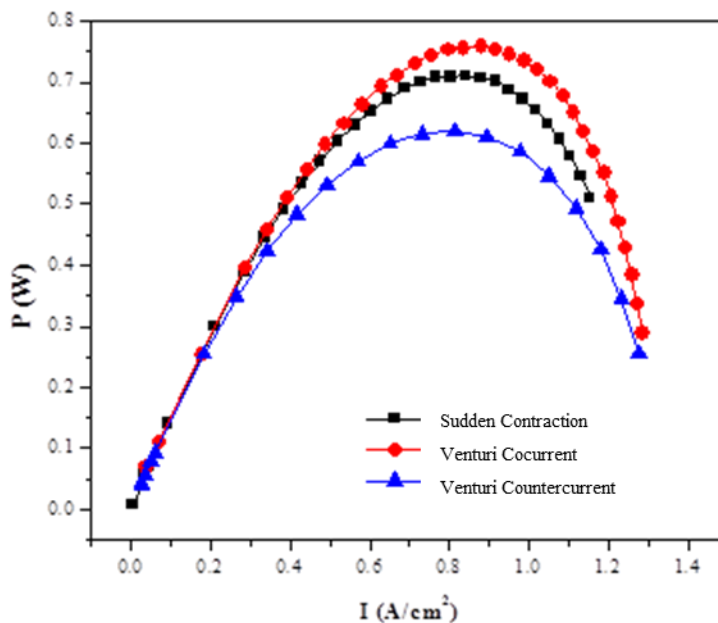


Figure 14. Power curves at 10 psi of cathodic pressure in the PEMFC with different structural arrays and flow patterns at the gas inlets to the polar plates.

Power curves for the various performance conditions described (Figure 9 - 12) are presented in Figure 13. When the PEMFC was equipped for VA and concurrent flow, the highest power output (approx. 0.68 W) was observed, at a current density of about 0.9 A/cm². This can be compared to the 0.62 W for SCA and 0.59 W for VA using countercurrent flow with the peaks occurring at about 0.75 A/cm² and 0.9 A/cm², respectively. Power curves intersections leading to improved output power for the countercurrent flow case were observed at current densities (0.98 & 1.3 A/cm²) when compared to SCA and VA concurrent flow respectively. These behaviors were attributed to better mass transport conditions as the membrane became fully hydrated.

Power curves for a PEMFC at 10 psi cathode pressure for the three test conditions are shown in Figure 14. An unexpected increase in the cell power for both the SCA and VA concurrent flow cases were observed, while VA using concurrent flow still produced the most power, and this peak was about 13% higher than that observed at the lower pressure (~ 0.77 W). Over the range of current densities tested, no power curve intersections were observed.

In Figure 15, power curves for the tested conditions at 14 psi cathode pressure are presented. This graph shows the best performance for the SCA concurrent flow system. The maximum power value (0.75 W) is observed at a current density about 0.9 A/cm² (a value slightly lower than observed at 10 psi for VA concurrent flow) but this higher cathodic pressure was not favorable for the VA geometry. Power performance was lowered in both from power peaks at lower pressure. For VA countercurrent flow, the peak was only 0.60 W (observed around 0.79 A/cm²) while it was much lower (0.63 W) for VA concurrent flow at about 0.75 A/cm². Finally, an intersection is observed at 1.1 A/cm², when VA countercurrent flow output exceeded VA-concurrent flow output, attributable to the improved mass transport conditions in PEMFC for the VA geometries discussed earlier.

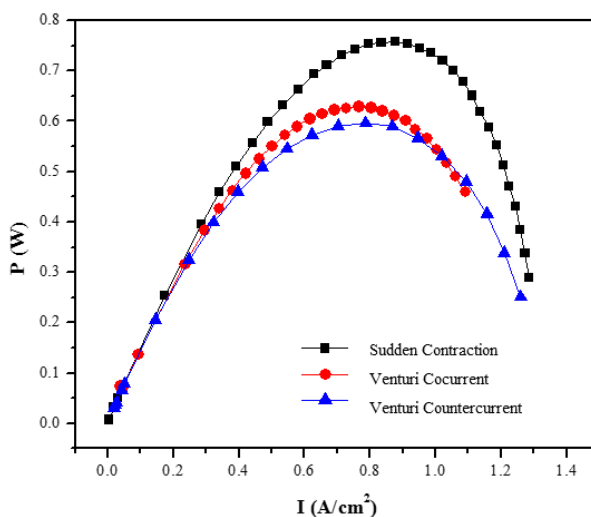


Figure 15. Power curves at 14 psi of cathodic pressure in the PEMFC with different geometry arrays and flow patterns for the inlet gases to the polar plates.

4. CONCLUSIONS

Results show that the specific structural intake and exhaust geometry (VA & SCA) for reactant gases affects the flow characteristics as gas velocity profiles, gas density, head losses and Reynolds number, however only relatively minor, and at times non-intuitive, effects was observed on PEMFC performance between these changing flow characteristics.

Additionally, some interesting effects on the PEMFC performance and power was observed when similar geometries, but with concurrent flow versus countercurrent flow, were observed. The team found that concurrent flow offered favorable effects on the activation and ohmic zones, resulting in significant differences on the performance and power curves at same operational conditions (for VA concurrent vs. VA countercurrent at about 0.9 A/cm^2 , the concurrent flow provided about 28% higher peak power). However, the countercurrent flow condition offered better performance once the diffusion zone of PEMFC performance and power curves were reached. These results contradict references. It is believed and proposed that these results can be understood when mass transfer through the gas distribution channels of the PEMFE are considered. Here the shape of gas distribution channels applied were typically wider and deeper than those used in other studies, and thus have an important role to play with water management inside the PEMFC when using countercurrent flow at the cathode. With the larger cross-section seen here, when operating at higher current densities, full membrane hydration was achieved (but was not at the lower current densities). Thus, under high cross section channel size and countercurrent flow the activation and ohmic losses on PEMFC performance were more severe until full hydration was achieved, when the diffusion resistance decreased at high current densities.

Based on the test results seen here, the team suggests that the best combination of operating conditions to employ for a PEMFC would be with high purity hydrogen and oxygen at a cathodic pressure of 10 psig using concurrent flow of the reactant gases. These operational conditions yield the best reported power performance ($\sim 0.78 \text{ W}$) at a current density of about 0.9 A/cm^2 .

References

1. F. Barbir, PEM Fuel Cells: Theory and Practice, *Elsevier Academic Press*. (2005) USA.
2. L. P. Jarvis, P. J. Cygan and M. P. Roberts, *IEEE Aerosp. Electron. Syst. Mag.* 18 (2003) 13.
3. M. Prigent, Les piles à combustible, Ed. Institut français du pétrole. (1997) Paris.
4. P. Costamagna P., S. Srinivasan, *J. Power Sources*, 102 (2001) 327.
5. V.S. Bagotzky, N.V. Osetrova and A. M. Skundin, *Russ J. Electrochem.*, 39 (2003) 1027.
6. P. Costamagna, S. Srinivasan, *J. Power Sources*, 102 (2001) 242.
7. A. T-Raissi, Current technology of fuel cell systems, International Energy Conversion Engineering Conference (IECEC), (1997) 1953.
8. Tae-Young Oh and Seok-Lyong Song, Present status and future of fuel Cell Development in Hyundai Heavy Industries, 1st *International Forum on Strategic Technology*, (2006) 209.

9. C. Moisés Bautista Rodríguez, M. G. Araceli Rosas Paleta, J. Antonio Rivera Márquez, A. Belén Tapia Pachuca, J. Roberto García de la Vega. *International Journal of Electrochemical Science* 4 (2009) 1754
10. C. Moisés Bautista Rodríguez, M. G. Araceli Rosas Paleta, J. Antonio Rivera Márquez, A. Belén Tapia Pachuca, J. Roberto García de la Vega. *Journal of New Materials for Electrochemical Systems*, 13 (2010) 261
11. C. Moisés Bautista-Rodríguez*, Araceli Rosas-Paleta, Andrés Rodríguez-Castellanos, J. Antonio Rivera-Márquez, Omar Solorza-Feria, J. Antonio Guevara-Garcia, J. Ignacio Castillo-Velázquez. *International Journal of Electrochemical Science*, 2 (2007) 820
12. U. Beuscher, *J. Electrochem. Soc.*, 153 (2006) 1788.
13. A. M. Ebesui, C.V. Boccuzzi, G. Ett, G. Janolio, G. Y. Saiki, J.A. Jardini, M. Ellem and V. Ett, Development and test of a proton exchange membrane fuel cell (PEMFC) for stationary generation, Transmission and Distribution Conferences and Exposition Latin America IEEE /PES. (2004) 605.
14. I. Sabir, L. Xianguo, Bipolar plates of PEMFC, Department of Mechanical Engineering University of Waterloo Fall. (2004).
15. R. Lawton, J.F. Bash and S.M. Barnett, Marine applications of fuel cells, Oceans/'02 MTS/ IEEET. (2002).
16. T. Susai, A. Kawakami, A. Hamada, Y. Miyake and Y. Azegami, *J. Power Sources*. 92 (2001) 99.
17. V. A. Paganin, F. A. Ticianelli and E. R. Gonzalez, *J. Power Sources*. 70 (1998) 55.
18. Kim J. Lee S-M, and S. Srinivasan, *J. Electrochem. Soc.* 142 (1996) 2668.
19. C.M. Bautista-Rodríguez, A. Rosas-Paleta, A. Rodríguez-Castellanos, J.A. Rivera-Márquez, O. Solorza-Feria, J.A. Guevara-Garcia and J.I. Castillo-Velázquez, *Int. J. Electrochem. Sci.* 2 (2007) 820.
20. C.J. Geankoplis, Transport Processes and Unit Operations, Ed. CECSA (1998) USA.
21. E.E. Ludwing, Applied Process Design for Chemical and Petrochemical Plants, Ed. Gulf Professional Publishing (1999) USA.
22. Crane, Flow fluids in valves, accessories and pipes. Ed. McGraw-Hill (1987) USA.
23. L. K. Kwac and Hong Gun Kim. *Journal of Mechanical Science and Technology* 22 (2008) 1561
24. M. Zeroual, H. Ben Moussa, M. Tamerabet. *Energy Procedia* 18 (2012) 317
25. A. Morin, F. Xu, G. Gebel, O. Diat. *Int. Journal of Hydrogen Energy* 36 (2011) 3096

© 2018 The Authors. Published by ESG (www.electrochemsci.org). This article is an open access article distributed under the terms and conditions of the Creative Commons Attribution license (<http://creativecommons.org/licenses/by/4.0/>).